

# Approximate Acoustic Boundary Conditions in the Time-Domain using Volume Penalization

Mathias Lemke and Julius Reiss

Fachgebiet Numerische Fluiddynamik, Technische Universität Berlin  
Müller-Breslau-Strasse 15, 10623 Berlin, Germany

Immersed boundary methods allow describing complex objects on simple Cartesian grids in time-domain simulations. The penalization technique employed here is a physically motivated Brinkman method that models objects as porous material by including a friction term and an effective volume. We investigate how the approach can mimic different acoustic boundary conditions. It is validated concerning different acoustic setups, including rigid walls and various absorber configurations.

## 1 Introduction

Acoustic time-domain simulations allow describing effects, which are difficult to include in geometrical acoustics, like diffraction or non-constant sound propagation velocities. These advantages often justify the high numerical effort compared with classical methods. That holds especially since the increasing computational resources permit practical calculations for frequencies above the Schroeder frequency on standard workstations.

Time-domain simulations can be based on the wave equation [14], the non-linear Euler equations [31, 32] or the acoustic equations as its linearized form. A variety of numerical methods has been utilized, like the finite-difference (FD) [4], the finite element (FEM) [5], the finite volume (FVM) [2] or the discontinuous Galerkin method (DG) [25].

In all these approaches, the boundary conditions are in particular decisive for the quality of the simulations [36]. Acoustic boundary conditions are often characterized by their impedance. However, the complex-valued variable is primarily suitable for frequency-based analyzes. A transfer to the time domain is difficult and the subject of current research [8, 20, 24, 25].

This article presents an immersed boundary method in the time domain, implemented via finite-differences, that is physically motivated and able to model objects with typical acoustic impedances. The approach is easy to use, computationally efficient, fully parallelizable, and does not need particular boundary adaptations of the grid.

Immersed boundary methods replace the enforcement of boundary conditions on grid lines or element boundaries by additional force-like terms in the governing equations. Various methods exist: The Brinkman volume penalization models objects as porous material and approximates solid objects for a vanishing porosity [21]. Among others, the approach is used in aeroacoustics [13]. Often two parameters model the effect of the porous material, a linear friction relative to the material (Darcy term) for the fluid velocity (becoming the particle velocity in a pure acoustic case), and the effective volume  $\phi$ , commonly called porosity in this context. The effective volume is included in the governing (flow) equations for flows differently by different authors as detailed in [12, 27]. The equations of [27] agree with

a model derived from a two phase flow description [11] and similar for mechanical waves in earth crust with complex typologies by [34]. The acoustic reflectivity of porous material is investigated in the time domain by [37]. Consistent treatment of the effective volume allows varying these two parameters largely independently over a wide range and thereby mimicking different boundary conditions [27]. Here an extended investigation of this approach for various acoustic boundary conditions is presented.

The manuscript is structured as follows: Section 2 introduces the governing equations. In Sec. 3 their numerical discretization is discussed. Section 4 presents validation results for rigid wall and absorber configurations as well as reactive boundaries in the form of Helmholtz resonators for different setups from 1-D to 3-D. A summary of the findings is given in Sec. 5. In the appendix a discussion on the use of the volume penalization approach within the wave equation is provided.

## 2 Governing Equations

The Euler-equations [15] are used as governing equations for acoustics as they comprise sound formation and propagation, including non-linear effects. The Brinkman penalization is introduced into the Euler-equations by an effective volume  $\phi$  [27] and a Darcy term proportional to  $\chi$  [13] on the right-hand-side to enable suitable impedance boundary conditions. The terms are highlighted in bold font.

$$\phi \partial_t(\rho) + \partial_{x_i}(\phi \rho u_i) = 0 \quad (1)$$

$$\phi \partial_t(\rho u_j) + \partial_{x_i}(\phi \rho u_i u_j) + \phi \partial_{x_j} p = \phi \chi(\mathbf{u}_j^t - \mathbf{u}_j) \quad (2)$$

$$\phi \partial_t(\rho e_t) + \partial_{x_i}(\phi \rho u_i e_t + \phi u_i p) = 0 \quad (3)$$

Therein,  $\rho$  denotes the density,  $u_j$  the velocity in  $x_j$ -direction,  $e_t$  the specific total energy,  $p$  the pressure and  $\gamma$  the heat capacity ratio. The value  $u_j^t$  corresponds to the velocity of the modeled boundary/object and is zero in the further course of this manuscript. We do not explicitly emphasize that the variables are functions of space and time for the sake of brevity. The sum convention applies for  $i, j = [1, 2, 3]$ . Assuming a constant heat capacity the energy equation can be reformulated using  $e_t = (p/\rho) \cdot 1/(\gamma - 1) + (u_j u_j)/2$  [18] resulting in

$$\phi \partial_t(p) + \gamma \partial_{x_i}(\phi u_i p) - (\gamma - 1) \phi u_i \partial_{x_i} p = 0. \quad (4)$$

The acoustic equations are provided in the appendix.

**Effective volume ( $\phi$ )** The inclusion of the effective volume  $\phi$  can be interpreted as an volume fraction  $\phi(x_i) = V_{\text{fluid}}/V_{\text{total}}$  caused by the presence of a porous medium. Thus, the value of  $\phi$  varies between 0 and 1. With  $\phi = 0$  the Euler equations (1)-(3) degenerate. This situation is avoided by choosing a small but finite value for  $\phi$  in the simulations. With  $\phi = 1$  the unmodified Euler equations are recovered, a spatial constant  $\phi$  can be factored out. Negative values or values greater than one are non-physical and are excluded. A time-dependent  $\phi$  is discussed in [11, 27] and not considered here.

Another interpretation of the effective volume  $\phi$  is a reduced cross-section of a stream tube. We will exploit this second interpretation when modelling Helmholtz resonators in Sec. 4.2.

An extensive discussion of the terms is carried out in [27, 11]. In particular, it is argued that the presence of the effective volume does not change the local speed of sound and interferes only slightly with the eigenvalues of the governing equations. Thus, existing aeroacoustic simulation programs can be reused by modifying the governing equations.

**Darcy term ( $\phi\chi(\mathbf{u}_j^t - \mathbf{u}_j)$ )** The momentum equations are expanded by a penalization of form ( $\phi\chi(\mathbf{u}_j^t - \mathbf{u}_j)$ ) with  $\chi(x_i) = \chi_x(x_i) \cdot \chi_s(x_i)$  controlling its spatial location  $\chi_x$  and strength  $\chi_s$ . This is referred to as Darcy-term in the following. The expression can be interpreted as velocity damping caused by the presence of a porous material. The target velocity  $\mathbf{u}_j^t$  corresponds to the velocity of the material and is chosen to zero in the following. While the location parameter  $\chi_x$  varies between 0 and 1, the strength parameter  $\chi_s$  varies between 0 and  $\infty$ . In the limit  $\chi_s \rightarrow \infty$  the Euler equations degenerate. For  $\chi = 0$  the force term vanishes. Larger values of  $\chi$  result in larger negative Eigenvalues of the right-hand-side operator, which has a corresponding influence on the stability of the numerical simulation or requires substantially smaller time steps for explicit time marching.

Regardless of this, it is possible to model solid/fully reflective or semi-permeable boundaries with sufficiently large values of  $\chi$  [13, 17], analogous to the effective volume. However, in the following,  $\phi$  is used to model solid walls and not a large Darcy term. In the validation examples, the values of  $\chi$  used for modeling practically relevant acoustic boundaries do not lead to restrictions in terms of stability and the time step, respectively.

The term usually added to the energy equation is dropped, as in the short computational time, no significant heat effects are expected [21, 17].

## 3 Numerical Discretization

### 3.1 Space discretization

The governing partial differential equations (1-3) are discretized using the finite difference approach in the

time-domain (FDTD) on an equidistant Cartesian grid. The spatial derivatives are approximated by finite differences. Explicit schemes, schemes that are optimized concerning the transmission behavior [33], implicit schemes [16] that include the solution of a linear system of equations, or spectral methods can be employed. In principle, all finite difference (FD) schemes are suitable for discretizing the governing equations.

The variables  $\phi(x_i)$  and  $\chi(x_i)$  are chosen to define an acoustic (and fluid dynamic) boundary condition. Both are field variables and can thereby have different values for each grid point. The values are motivated by physics and can be estimated from material properties, see below. The effective volume in  $\phi$  is identified as the volume not occupied by a porous material or a resonator. The variable  $\chi$  corresponds to the flow resistivity. Initial guesses by the physical quantities provide approximations that are often good enough for basic applications. Thus, the Brinkman penalization is not a first-principles approach but an approximate description.

### 3.2 Time discretization

Throughout this manuscript, the time is discretized by the standard explicit Runge-Kutta-4 (RK4) method [30]. As an explicit method, it is easy to implement but restricts the maximal time-step. The eigenvalues of the spatially discretized equations scaled by the time-step must be within the so-called stability region [30] of the method. For the inviscid problems of acoustics, the time-step can be estimated by the CFL number  $\frac{c\Delta t}{\Delta x} \leq \text{CFL}_{\text{max}}$ , where  $\Delta x$ ,  $\Delta t$  are the spatial and temporal discretization,  $c$  is the speed of sound and  $\text{CFL}_{\text{max}}$  is a limit depending on details of the discretization which is usually of the order of one.

Large values of  $\chi_s$  increase the eigenvalues and thus reduce the permitted time step  $\Delta t$ . Sharp spatial changes in  $\phi$  do have a similar effect, whereas a smoothing to distribute the change over a few grid points avoids such a restriction [27].

Larger values of the Darcy term or sharper changes of  $\phi$  could be handled by an implicit or semi-implicit method as used in [3]. A large  $\chi_s$  corresponds to simply setting the target values inside rigid objects. This reduces the smoothness of the solution having a detrimental effect on the discrete solution [7, 23]. For realistic porous materials, the values of  $\chi$  are low, and no restriction of the time-step is expected.

To ensure numerical stability, a spatial filter can be used. In some examples in Sec. 4, a compact filter following [9] is employed. However, a standard filter can result in a conservation defect for a non-constant effective volume  $\phi$ , which is usually not essential for acoustic simulations. A conservative filter with varying  $\phi$  is discussed in [27].

### 3.3 Blending functions

The values  $\phi$  need to be smoothed to avoid numerical problems like stiffness [27]. In this publication the smoothing is done by a hyperbolic tangent function, e.g.

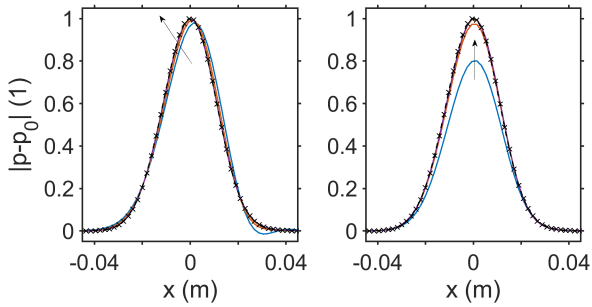


Figure 1: (color online) Reflected pressure pulse in comparison to a reference (black, dashed with crosses representing the grid points) created by a mirror pulse, both normalized with respect to the ambient pressure  $p_0$  and the maximum amplitude. (Left) Change of the reflected pulse with  $\delta = 2.0\Delta x, 1.5\Delta x, 1.0\Delta x, 0.5\Delta x$ , using  $\phi_\epsilon = 10^{-3}$ . The phase error increases with  $\delta$ . (Right) Change of the reflected pulse for  $\phi_\epsilon = 10^{-1}, 10^{-2}, 10^{-3}, 10^{-4}$  using  $\delta = 1\Delta x$ . For an increasing  $\phi_\epsilon$  the reflected wave becomes smaller in amplitude.

for a wall at position  $x_0$  the effective volume is given by

$$\phi(x) = 1 - (1 - \phi_\epsilon)(\tanh((x - x_0)/\delta) + 1)/2. \quad (5)$$

Here  $\delta$  determines the smoothing width and  $\phi_\epsilon$  the residual volume of the wall. The smoothing influences the acoustic behavior of the boundary. It is tested with an adiabatic Gaussian pulse  $p = \exp(-x^2/\sigma_{\text{pulse}}^2)$ , with  $\sigma_{\text{pulse}} = 8\Delta x$ , with the grid spacing  $\Delta x$ . The results are computed using a standard fourth-order FD derivative and the RK4 with a CFL number of  $\approx 0.7$ .

The smoothing of  $\phi$  yields a different penetration depth for different wavenumbers, becoming larger with larger  $\delta$ , visible as a dissipation-like error, see Fig. 1, left. It can be shown that the error is dominantly a phase error [27] for small  $\phi_\epsilon$ . A small value of  $\phi_\epsilon$  is desired for a rigid wall. If it is not close to zero only a partial reflection of the acoustic wave results, see Fig. 1, right. In combination with a suitable Darcy term, this can be used to create partially reflecting walls.

A combination of a small  $\phi_\epsilon$  and a small  $\delta$ , is implied for a rigid wall. However, such a combination makes the equations stiff and thereby severely restricts the time step. If a total reflection is not essential (for example, to reproduce theoretical cases), a value of  $\phi_\epsilon \sim 10^{-3}$  and a  $\delta = 0.5\Delta x$  seem a good compromise, as this allows to keep nearly the original time step. For realistic rigid walls, even a lower reflectivity and thereby a larger  $\phi_\epsilon$  seems adequate.

Functions other than the hyperbolic tangent function can be used for smoothing. The error function erf was tested, but found to produce stiffer problems. No extensive study was carried out on this aspect since the hyperbolic tangent produces satisfactory results.

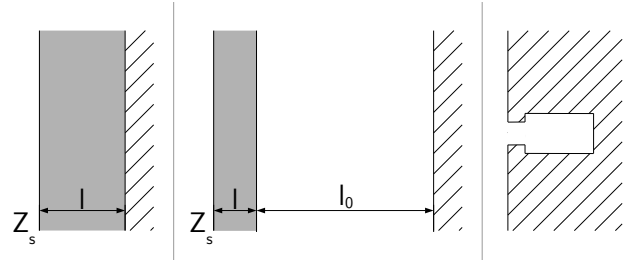


Figure 2: Acoustic configurations: (A1, left) Porous material, mounted on a rigid wall. (A2, center) Porous material mounted in front of an air cavity. (B, right) Model representation of a resonator.

Table 1: Parameters of the absorber configuration used for validation.

	material thickness	air cavity depth	flow resistivity
	$l$ (m)	$l_0$ (m)	$\sigma$
A1	0.1	0	3000
A2	0.05	0.15	14400

## 4 Numerical validation examples

In the following, the Brinkman penalization approach for the representation of acoustic wall boundary conditions is validated using different examples. This includes various configurations with absorbers and rigid walls, examined in several dimensions. Figure 2 shows the basic structure of the absorbers and the resonator examined below. The key figures of the absorbers are shown in Tbl. 1.

If the impedance is the goal of the validation, the numerically resulting surface impedance is compared with the analytical solution according to the Miki model [22, 28]. Therein, the characteristic impedance  $Z_c$  is given by

$$Z_c = \rho c \left( 1 + 0.070 \left( \frac{f}{\sigma} \right)^{-0.632} - 0.107\sqrt{-1} \left( \frac{f}{\sigma} \right)^{-0.632} \right) \quad (6)$$

with  $c$  as the speed of sound,  $f$  as frequency, and  $\sigma$  as flow resistivity.

Assuming a plane wave the surface impedance of porous material backed by another material is given by [25] as

$$Z_s(\phi) = \frac{Z_c k_t}{k_x} \left( \frac{-\sqrt{-1}Z_b \cot(k_x l) + Z_c \frac{k_t}{k_x}}{Z_b - \sqrt{-1}Z_c \frac{k_t}{k_x} \cot(k_x l)} \right). \quad (7)$$

Therein,  $l$  denotes the thickness of the porous material, and  $\phi$  is the incidence angle with respect to the porous

surface. The wavenumber  $k_t$  is defined as

$$k_t(f) = \frac{2\pi f}{c} \left( 1 + 0.109 \left( \frac{f}{\sigma} \right)^{-0.618} - 0.160\sqrt{-1} \left( \frac{f}{\sigma} \right)^{-0.618} \right) \quad (8)$$

with  $k_x = \sqrt{k_t^2 - k^2 \sin^2(\phi)}$  and  $k$  as free space wavenumber.

In case the porous material is backed by a rigid wall, see Fig. 2 (left), the surface impedance reduces to

$$Z_s(\phi) = -\sqrt{-1} Z_c \left( \frac{k_t}{k_x} \right) \cot(k_x l). \quad (9)$$

If there is an air cavity between the porous material and the wall, see Fig. 2 (center),

$$Z_b = -\rho c \sqrt{-1} \frac{\cot(k_0 \cos(\phi) l_0)}{\cos(\phi)} \quad (10)$$

holds with  $l_0$  as the thickness of the cavity.

#### 4.1 1D - absorber

As first validation cases, the absorber configurations A1 and A2 are examined. The 1-D computational domain with a length of 2.5 m is discretized with 626 equidistantly distributed points. An explicit 4th order derivative is used. An explicit 4th order Runge-Kutta method is used for temporal integration. 20990 time steps are calculated at a sampling rate of 96 kHz. The resulting CFL number is 0.89. Characteristic non-reflecting boundary conditions [35, 26] are imposed on both sides of the computational domain. An acoustic source is imposed at the coordinate  $x_1 = 0.4$  m during the entire computational time. Its signal is given by a linear chirp from 50 to 3500 Hz over the simulation time.

Both absorber configurations are modeled by a suitable choice of the effective volume  $\phi$  and the Darcy penalization  $\chi$ . The functions are given by:

$$\begin{aligned} \phi(x) = 1 - \frac{(1 - \phi_p)}{2} & \left[ (\tanh((x - s_p)/\delta)) \right. \\ & \left. - (\tanh((x - e_p)/\delta)) \right] \\ & - \frac{(1 - \phi_w)}{2} \left[ (\tanh((x - s_w)/\delta)) \right. \\ & \left. - (\tanh((x - e_w)/\delta)) \right] \end{aligned} \quad (11)$$

and

$$\begin{aligned} \chi(x) = + \frac{a_p}{2} & \left[ (\tanh((x - s_p)/\delta)) \right. \\ & \left. - (\tanh((x - e_p)/\delta)) \right] \\ & + \left[ (\tanh((x - s_w)/\delta)) \right. \\ & \left. - (\tanh((x - e_w)/\delta)) \right]. \end{aligned} \quad (12)$$

The values for the spatial parameters start ( $s$ ) and end ( $e$ ) of the absorber material  $\bullet_p$  and the backing wall  $\bullet_w$  are stated in Tbl. 2. The steepness of the tanh-flanks is controlled using a value of  $1.5\Delta x$  for the parameter

Table 2: Parameters of effective volume and Darcy penalization for configurations A1 and A2.

	effective volume			Darcy penalization			
	$s_w$	$e_w$	$\phi_w$	$s_p$	$e_p$	$a_p$	$\phi_p$
A1	2.115	$\infty$	$10^{-6}$	2.0	2.100	4300	1.0
A2	2.212	$\infty$	$10^{-6}$	2.0	2.056	12500	1.0

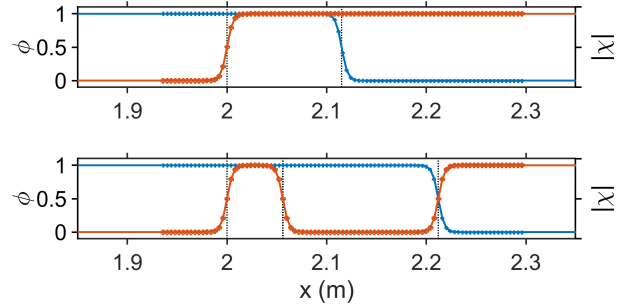


Figure 3: (color online) Resulting curves for the effective volume ( $\phi$ , blue) and the penalization ( $\chi$ , red) for the cases A1 (top) and A2 (bottom). The course for  $\chi$  is normalized with the respective amplitude  $a_p$ . The vertical lines correspond to turning points in the profiles. The markers correspond to the grid points in the finite-difference grid used.

$\delta$ . Please note that in general,  $\delta$  can be chosen independently for both functions  $\phi$  and  $\chi$ .

The resulting curves for the effective volume  $\phi$  and the Darcy term are shown in Fig. 3.

The values are adjusted manually to achieve a good match with the validation reference. A detailed optimization was not carried out. The values are similar to the reference values.

The resulting (normal incidence) surface impedance is computed using  $Z_s = \hat{p}/\hat{u}$ , where  $\hat{p}$  and  $\hat{u}$  are the Fourier transformed pressure and velocity time responses at position  $x = s_p$ . In comparison to the impedance based on the Miki-model a good agreement is found, see Fig. 4.

We conclude that the Brinkman penalization approach can mimic acoustic absorber configurations very well with a small adaption of the modeling parameters.

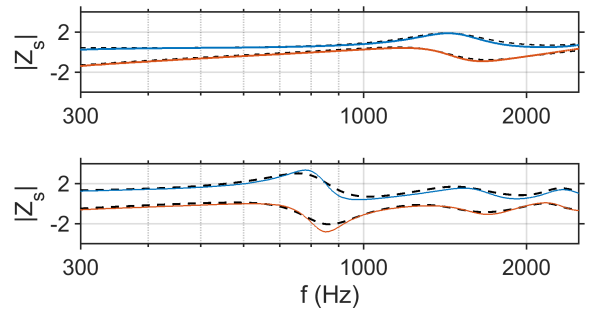


Figure 4: (color online) Resulting surface impedance  $Z_s$  normalized with  $\rho c$  for the cases A1 (top) and A2 (bottom) - real (blue) and imaginary part (red) compared to the analytical solution according to the Miki model.

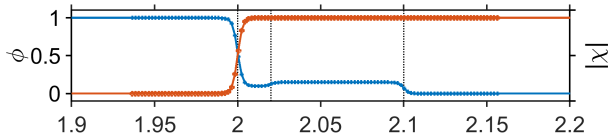


Figure 5: (color online) Resulting curves for the effective volume ( $\phi$ , blue) and the penalization ( $\chi$ , red) for the reactive surface B. The course for  $\chi$  is normalized with respect to the maximal amplitude. The vertical lines correspond to turning points in the tanh-functions, defining the neck and the resonator volume. The markers correspond to the grid points in the finite-difference grid used.

## 4.2 1D - responsive surface

The numerical case B considers a responsive surface. The underlying idea is that the effective volume of the porosity can be interpreted as a channel with varying cross-sections [1, 27].

The 1-D computational domain with a length of 2.5 m is discretized with 1252 equidistantly distributed points. Again, an explicit 4th order derivation scheme and an explicit 4th order Runge Kutta method are used for discretization. 20990 time steps are calculated at a sampling rate of 192 kHz. The resulting CFL number is 0.89. Characteristic non-reflecting boundary conditions are imposed on both sides of the computational domain. An acoustic source is imposed at the coordinate  $x_1 = 0.2$  m during the entire computational time. As before, its signal is given by a linear chirp from 50 to 3500 Hz over the computational time.

The effective volume and the Darcy penalization are chosen to mimic an acoustic element containing a Helmholtz resonator. In detail, tanh-functions are used to model the neck and the resonator volume of the acoustic element. A value of  $\delta = 1.5\Delta x$  is again chosen as the steepness of the flanks of  $\phi$  and  $\chi$ . The neck starts at 2 m and ends at 2.02 m, where the resonator volume with a length of 0.08 m volume starts. Behind the resonator, the wall is modeled to begin at 2.1 m. Within the neck, the effective volume is set to 0.1, while it is increased for the resonator volume to 0.15. To mimic the wall,  $\phi$  is set to  $10^{-6}$  in the corresponding wall region. The Darcy penalization is chosen to a maximum value of 250 starting at the neck. The resulting curves for the effective volume and the penalization are shown in Fig. 5.

The resulting acoustic properties of the model are validated by comparison of the impedance  $Z_s = \hat{p}/\hat{u}$  at the neck entry and the analytic impedance of an Helmholtz resonator given by [6]

$$Z_{s,HR} = R_l + \sqrt{-1} \frac{\rho H}{\omega S} \left( \omega^2 - \frac{c^2 S}{VH} \right) \quad (13)$$

or the corresponding reflection coefficient  $R = (Z/(qc) - 1)/(Z/(qc) + 1)$  respectively. Therein,  $R_l$  denotes an additional damping coefficient,  $H$  the neck length,  $S$  the diameter of the neck tube, and  $V$  the volume of the resonator. The corresponding values for the case examined, here, are shown in Tbl. 3.

Table 3: Parameters of the model for an acoustic element used to describe configuration B.

$H$	$S$	$V$	$R_l$
0.0367	0.0205	0.0025	1850

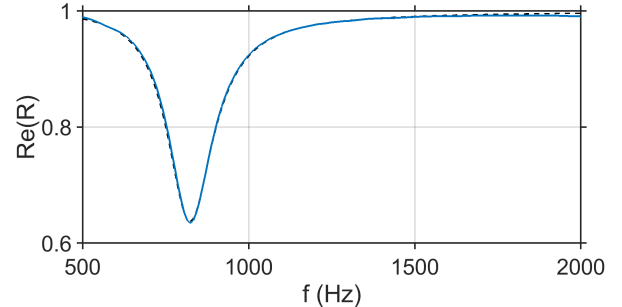


Figure 6: (color online) Progress of the reflection coefficient (blue) for configuration B compared to the analytical solution of an acoustic element (black, dashed).

As before, the parameters have been adjusted to obtain a good match. A detailed optimization was not carried out.

Please note that the values in the 1-D-model examined here have no direct physical equivalence. Nevertheless, the comparison of the Brinkman penalization approach and the analytical solution shows a very good agreement, see Fig. 6.

The Brinkman penalization can mimic responsive boundary conditions. However, in the course of the manuscript, only passive wall impedance boundary conditions will be examined further.

## 4.3 2D - Circular Domain

In the following, a 2-D circular domain is considered. The dimensions of the computational domain are  $0 \leq x_1 \leq 1.4$  m and  $0 \leq x_2 \leq 1.4$  m. A uniform grid with  $145 \times 145$  points is used. A fourth-order accurate symmetric derivation stencil is employed. The computational time of 3 s is separated into 144000 time steps which result in a CFL condition of 0.735. An explicit fourth-order Runge-Kutta scheme is used for the time integration. All domain-boundaries are treated as non-reflecting using characteristic boundary conditions [35, 26]. Since the boundary condition is in the modeled wall no substantial influence on the results is expected. To ensure stability, an implicit filter of 4th order is employed at each time step [9]. The simulation is initialized with a Gaussian pulse with a spatial variance of 0.05 at  $x_1 = 1.0$  m and  $x_2 = 0.8$  m.

The circular geometry is modeled by the Brinkman penalization approach, see Fig. 7. The effective volume  $\phi$  is varied between  $\phi_p$  and 1 using the following formula

$$\phi(r) = 1 - \frac{(1 - \phi_p)}{2} \left( \tanh \left( \frac{r - 0.5}{\delta} \right) + 1 \right). \quad (14)$$

Therein  $\phi_p = 10^{-5}$  denotes the minimal value of the effective volume and  $r$  the radial distance of each grid

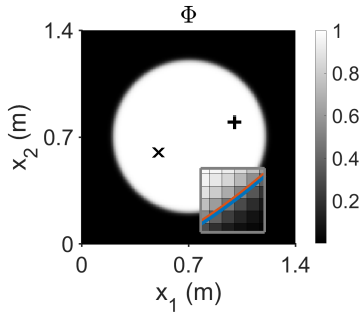


Figure 7: (color online) Spatial distribution of the effective volume  $\phi$  in setup C. The source position and the receiver positions are marked by + and x, respectively. The inset shows the  $\phi$  distribution zoomed in the wall area. Turning point of the function selected at a distance of half a meter from the center (red). Resulting room size for a good match of the room modes (blue), see text for more details.

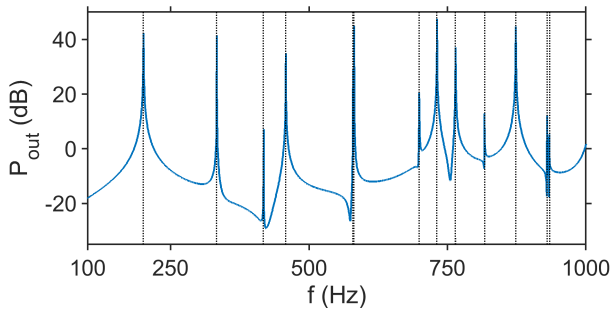


Figure 8: (color online) Frequency responses (blue) in the 2-D-circular C domain using the volume penalization approach. Analytic modes are presented by vertical lines (black, dashed), calculated using Green's function. Note that also double peaks are slightly visible.

point to the center of the domain. A value of  $\delta = 1.75\Delta x$  is chosen as the steepness of the flank. There is no Darcy penalization so that  $\chi = 0$  applies to the entire domain.

A comparison of the resulting frequency responses, evaluated at the spatial location  $x_1 = 0.5$  m and  $x_2 = 0.6$  m with the analytical ones, given by roots of the derivative of the Bessel function [10, p. 110f], shows a good agreement, see Fig. 8. Also, frequencies that are very close together are correctly identified and separated. However, the analytical solution must be corrected to obtain the results. The analytical radius is increased by 0.2% of the actual dimension. The deviation is due to the approximate character of the penalization approach. However, the deviation is small and corresponds to about  $0.1\Delta x$ .

The Brinkman penalization can model non-grid-aligned geometries with good quality and, in particular, without complex adaptations of the computational grid as in [24]. The geometry is fully encoded in the values of  $\phi$  and  $\chi$  which are created once at simulation start. Thus, complex rooms are modeled without the need to evaluate surface elements in every time step which can be expensive for complex structures [36].

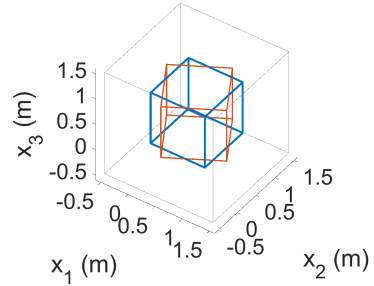


Figure 9: (color online) Edges of the room D modeled by the effective volume approach. Edges parallel to the computational grid (blue). Edges rotated by  $30^\circ$  with respect to the z-axis with the center point unchanged (red).

#### 4.4 3D - reverberation chamber

For this case, a three-dimensional cubic domain is considered. The dimensions of the computational domain are  $-0.5 \leq x_i \leq 1.5$  m for all three spatial directions. A uniform grid with  $201 \times 201 \times 201$  points is used. For the spatial discretization, a fourth-order accurate implicit symmetric derivation stencil is used [16]. The computational time of 3 s is separated into 144000 time steps which result in a CFL condition of 0.715. An explicit fourth-order Runge-Kutta scheme is employed for the time integration. All domain-boundaries are treated as non-reflecting using characteristic boundary conditions [35, 26]. The simulation is initialized with a Gaussian pulse with a full width at half maximum of  $2\Delta x_i$  at  $x_1 = 0.25$  m,  $x_2 = 0.75$  m and  $x_3 = 0.60$  m.

The room geometry is modeled using the effective volume  $\phi$  only. No Darcy penalization is applied. Thus,  $\chi = 0$  applies in the whole computational domain. The function  $\phi$  is varied between a minimum value of  $10^{-5}$  and 1 employing tanh-functions as above. The functions define a rectangular room with the dimensions  $1 \times 1 \times 1$  meters, centered in the computational domain. The locations of the boundary lines are shown in Fig. 9. A value of  $\delta = 1.75\Delta x$  is chosen as the steepness of the flanks. Two cases are investigated. In the first case, the edges of the room and the computational grid are parallel to each other. In the second case, the room is rotated by  $30^\circ$  with respect to the  $x_3$ -axis, whereby the center of the room remains unchanged.

A comparison of the resulting frequency responses, evaluated at the spatial location  $x_1 = 0.85$ ,  $x_2 = 1.30$  and  $x_3 = 0.80$  m with the analytical ones [29] and a simulation using fully reflecting boundary conditions show a very good agreement, see Fig. 10. That applies in particular to the rotated room, which shows that no alignment of the grid to the immersed boundary is necessary. Again, the room size in the analytical solution must be adapted to obtain the present result. The edge lengths of the analytical room are assumed to be 0.2% longer. The deviation corresponds to about  $0.2\Delta x_i$ . A similar offset was observed in [27] and could be compensated in the setup of the simulation.

The Brinkman penalization approach enables the sim-



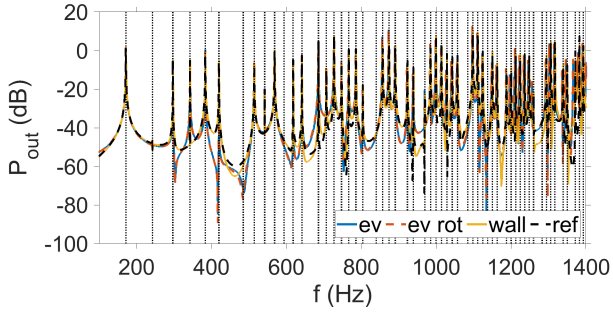


Figure 10: (color online) Frequency responses in the square 3-D domain (D) under consideration. FDFD-domain results using rigid boundary conditions (yellow), using the effective volume (blue), the effective volume under  $30^\circ$  rotation (red, dashed), and the analytical solution (black, dashed). The analytical eigenmodes are shown by vertical lines (black, dotted).

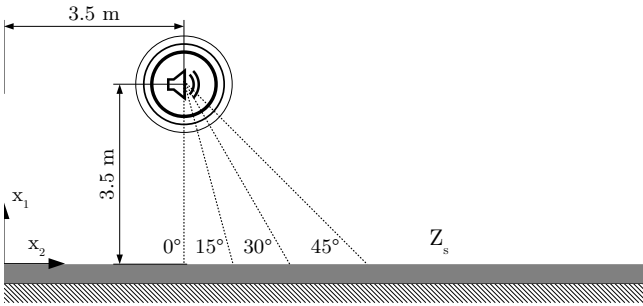


Figure 11: 2-D-section of the three-dimensional computational domain E at  $x_3 = 5$  m.

ulation of three-dimensional acoustic configurations. An alignment of the penalization concerning the computational grid is not necessary.

#### 4.5 3D - absorber - angle dependence

In the following, the angle dependency of the surface impedance of configuration A1 using the Brinkman penalization is examined. A 3-D domain is considered. The dimensions of the computational domain are  $-0.5 \leq x_1 \leq 6.5$  m,  $0.0 \leq x_2 \leq 10.0$  m and  $0.0 \leq x_3 \leq 10.0$  m. A uniform grid with  $700 \times 1000 \times 1000$  points is used. For the spatial discretization, a fourth-order accurate implicit symmetric derivation stencil was used [16]. The computational time is separated into 1500 time steps using a step width of  $\Delta t = 1/48000$  s. The CFL condition is 0.715. An explicit fourth-order Runge-Kutta scheme is employed for the time integration. All domain-boundaries are treated as non-reflecting using characteristic boundary conditions [35, 26]. The calculation is carried out in parallel on 80 cores, using the computational aeroacoustic framework presented in [19]. The simulation is initialized with a pressure Gaussian pulse with a sigma of 0.05 at  $x_1 = 3.5$ ,  $x_2 = 3.5$  and  $x_3 = 5.0$  m.

The absorber is modeled using the effective volume  $\phi$  and the Darcy penalization  $\chi$ . The courses of the function correspond to the case A1, shown in Fig. 3

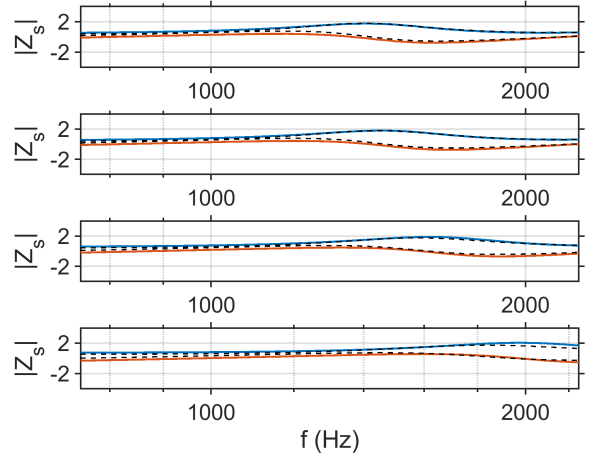


Figure 12: (color online) Resulting surface impedance  $Z_s$  for different incidence angles in setup E (top to bottom:  $0^\circ$ ,  $15^\circ$ ,  $30^\circ$ ,  $45^\circ$ ) normalized with  $\rho c$  - real (blue) and imaginary part (red) compared to the analytical solution (black, dashed) according to the Miki model.

(top). The surface of the porous material is located at  $x_1 = 0$  m, see Fig. 11.

To analyze the angle dependence of the penalization method, the wall impedance is evaluated at different points on the absorber surface at  $x_1 = 0$ , see Fig. 11. The impedance  $Z_s = \hat{p}/\hat{u}$  is compared with the analytical model (9). Corresponding curves for four angles from 0 to  $45^\circ$  are shown in Fig. 12. A good match is found. Please note that plane waves are assumed in the reference model used, which is only approximated in the performed numerical simulation.

The Brinkman penalization can mimic the angle dependence of the wall impedance of a typical absorber configuration.

## 5 Summary

A Brinkman penalization method for the approximate representation of acoustic wall boundary conditions was presented. The approach allows the realization of damping as well as responsive boundary conditions. The effective volume and the Darcy penalization are easy to interpret. The approach is fully parallelizable and easy to implement in existing time-domain simulation codes. Compared to other methods, there is no need for complex grid adaptations. The use of the effective volume does not lead to any significant limitation of the time step. The same applies to the Darcy terms as long as typical acoustic configurations are considered. The location of boundaries is changed by the smoothing of the modeling functions. However, a simple adjustment in the context of 1-D examinations is possible and can be transferred to 2 and 3 dimensions.

Through the spatial distribution of the penalization terms, a large number of degrees of freedom is available which allows the model to be adapted to experimental data as well as the simple optimization of impedance wall boundary conditions. The latter is the goal of fu-

ture research.

## Acknowledgments

The authors acknowledge financial support by the Deutsche Forschungsgemeinschaft (DFG) within the project LE 3888/2.

## A Acoustic Equations

The acoustic equations are derived from the Euler equations (1-2, 4) by linearization. Inserting  $p = p_0 + p'$ ,  $u = u_0 + u'$  and  $\rho = \rho_0 + \rho'$ , and keeping only terms linear in the fluctuations, yields

$$\phi\rho_0\partial_t(u') + \phi\partial_x(p') = \phi\chi(\mathbf{u}^t - \mathbf{u}') \quad (15)$$

$$\phi\partial_t(p') + p_0\gamma\partial_x(\phi u') = 0, \quad (16)$$

where  $u_0 = 0$  and constant  $\rho_0$  and  $p_0$  are assumed. The mass equation (1) can be ignored if adiabatic flows are assumed, as usually done for acoustic applications. The two equations can be combine with  $\partial_t\phi = 0$  to

$$\phi\partial_t^2(p') - c^2\partial_x(\phi\partial_x(p')) = -\partial_x\phi\chi(\mathbf{u}^t - \mathbf{u}') \quad (17)$$

This reveals that the usual wave equation with the wave velocity  $c$  is recovered in areas with constant  $\phi$ . Rewriting the term  $\partial_x(\phi\partial_x(p')) = \partial_x(\partial_x(p')) + (\partial_x p')(\partial_x\phi)$  allows to obtain a standard Laplacian. For computational purposes the form (15,16) is preferred as it avoids second derivatives.

## References

- [1] N. Andrianov and G. Warnecke. The riemann problem for the baer–nunziato two-phase flow model. *Journal of Computational Physics*, 195(2):434–464, 2004.
- [2] S. Bilbao. Modeling of complex geometries and boundary conditions in finite difference/finite volume time domain room acoustics simulation. *IEEE Transactions on Audio, Speech, and Language Processing*, 21(7):1524–1533, 2013.
- [3] O. Boiron, G. Chiavassa, and R. Donat. A high-resolution penalization method for large mach number flows in the presence of obstacles. *Computers & Fluids*, 38(3):703 – 714, 2009.
- [4] D. Botteldooren. Acoustical finite-difference time-domain simulation in a quasi-cartesian grid. *The Journal of the Acoustical Society of America*, 95(5):2313–2319, 1994.
- [5] A. Craggs. A finite element method for the free vibration of air in ducts and rooms with absorbing walls. 173(4):568–576, 1994.
- [6] K. Ehrenfried. *Strömungakustik: Skript zur Vorlesung*. Berliner Hochschulkripte. Mensch-und-Buch-Verlag, 2004.
- [7] T. Engels, D. Kolomenskiy, K. Schneider, and J. Sesterhenn. Numerical simulation of fluid–structure interaction with the volume penalization method. *Journal of Computational Physics*, 281:96–115, 2015.
- [8] K.-Y. Fung and H. Ju. Time-domain impedance boundary conditions for computational acoustics and aeroacoustics. *International Journal of Computational Fluid Dynamics*, 18(6):503–511, 2004.
- [9] D. V. Gaitonde and M. R. Visbal. Pade-type higher-order boundary filters for the navier-stokes equations. *AIAA Journal*, 38:2103–2112, Nov. 2000.
- [10] F. Jacobsen and P. M. Juhl. *Fundamentals of general linear acoustics*. John Wiley & Sons, 2013.
- [11] F. Kemm, E. Gaburro, F. Thein, and M. Dumbser. A simple diffuse interface approach for compressible flows around moving solids of arbitrary shape based on a reduced baer–nunziato model. *Computers & Fluids*, 204:104536, 2020.
- [12] N. K. Kevlahan, T. Dubos, and M. Aechtner. Adaptive wavelet simulation of global ocean dynamics using a new brinkman volume penalization. *Geoscientific Model Development*, 8(12):3891, 2015.
- [13] R. Komatsu, W. Iwakami, and Y. Hattori. Direct numerical simulation of aeroacoustic sound by volume penalization method. *Computers & Fluids*, 130:24 – 36, 2016.
- [14] K. Kowalczyk and M. van Walstijn. Room acoustics simulation using 3-d compact explicit fdtd schemes. *IEEE Transactions on Audio, Speech, and Language Processing*, 19(1):34–46, 2011.
- [15] L. D. Landau and E. M. Lifshitz. *Fluid Mechanics, Second Edition: Volume 6 (Course of Theoretical Physics)*. Course of theoretical physics / by L. D. Landau and E. M. Lifshitz, Vol. 6. Butterworth-Heinemann, 2 edition, Jan. 1987.
- [16] S. K. Lele. Compact finite difference schemes with spectral-like resolution. *Journal of Computational Physics*, 103(1):16 – 42, 1992.
- [17] M. Lemke, V. Citro, and F. Giannetti. External acoustic control of the laminar vortex shedding past a bluff body. *Fluid Dynamics Research*, 53(1):015506, feb 2021.
- [18] M. Lemke, J. Reiss, and J. Sesterhenn. Adjoint based optimisation of reactive compressible flows. *Combustion and Flame*, 161(10):2552 – 2564, 2014.
- [19] M. Lemke and L. Stein. Adjoint-based identification of sound sources for sound reinforcement and source localization. In R. Radespiel and R. Semaan, editors, *Fundamentals of High Lift for Future Civil Aircraft: Contributions to the Final Symposium of the Collaborative Research Center 880, December 17-18, 2019, Braunschweig, Germany*, pages 263–278. Springer International Publishing, 2021.



- [20] X. Li, X. Li, and C. Tam. Construction and validation of a broadband time domain impedance boundary condition. In *17th AIAA/CEAS Aeroacoustics Conference (32nd AIAA Aeroacoustics Conference)*, page 2870, 2011.
- [21] Q. Liu and O. V. Vasilyev. A brinkman penalization method for compressible flows in complex geometries. *Journal of Computational Physics*, 227(2):946 – 966, 2007.
- [22] Y. Miki. Acoustical properties of porous materials-modifications of delany-bazley models. *Journal of the Acoustical Society of Japan (E)*, 11(1):19–24, 1990.
- [23] R. Nguyen van yen, D. Kolomenskiy, and K. Schneider. Approximation of the laplace and stokes operators with dirichlet boundary conditions through volume penalization: a spectral viewpoint. 128(2):301–338.
- [24] F. Pind, A. P. Engsig-Karup, C.-H. Jeong, J. S. Hesthaven, M. S. Mejlum, and J. Strømmand-Andersen. Time domain room acoustic simulations using the spectral element method. *The Journal of the Acoustical Society of America*, 145(6):3299–3310, 2019.
- [25] F. Pind, C.-H. Jeong, A. P. Engsig-Karup, J. S. Hesthaven, and J. Strømmand-Andersen. Time-domain room acoustic simulations with extended-reacting porous absorbers using the discontinuous galerkin method. *The Journal of the Acoustical Society of America*, 148(5):2851–2863, 2020.
- [26] T. Poinsot and S. Lele. Boundary conditions for direct simulations of compressible viscous flows. *Journal Computational Physics*, 101:104–129, 1992.
- [27] J. Reiss. Pressure-tight and non-stiff volume penalization for compressible flows. *Journal of Scientific Computing*, 90(3):1–29, 2022.
- [28] A. Richard, E. Fernandez-Grande, J. Brunskog, and C.-H. Jeong. Estimation of surface impedance at oblique incidence based on sparse array processing. *The Journal of the Acoustical Society of America*, 141(6):4115–4125, 2017.
- [29] S. Sakamoto. Phase-error analysis of high-order finite difference time domain scheme and its influence on calculation results of impulse response in closed sound field. *Acoustical Science and Technology*, 28(5):295–309, 2007.
- [30] H. R. Schwarz and N. Koeckler. *Numerische Mathematik*. Springer-Verlag, 2009.
- [31] L. Stein, F. Straube, J. Sesterhenn, S. Weinzierl, and M. Lemke. Adjoint-based optimization of sound reinforcement including non-uniform flow. *The Journal of the Acoustical Society of America*, 146(3):1774–1785, 2019.
- [32] L. Stein, F. Straube, S. Weinzierl, and M. Lemke. Directional sound source modeling using the adjoint euler equations in a finite-difference time-domain approach. *The Journal of the Acoustical Society of America*, 148(5):3075–3085, 2020.
- [33] C. K. Tam and J. C. Webb. Dispersion-relation-preserving finite difference schemes for computational acoustics. *Journal of Computational Physics*, 107(2):262 – 281, 1993.
- [34] M. Tavelli, M. Dumbser, D. E. Charrier, L. Rannabauer, T. Weinzierl, and M. Bader. A simple diffuse interface approach on adaptive cartesian grids for the linear elastic wave equations with complex topography. *Journal of Computational Physics*, 386:158–189, 2019.
- [35] K. W. Thompson. Time dependent boundary conditions for hyperbolic systems. *Journal of Computational Physics*, 68(1):1 – 24, 1987.
- [36] M. Vorländer. Computer simulations in room acoustics: Concepts and uncertainties. *The Journal of the Acoustical Society of America*, 133(3):1203–1213, 2013.
- [37] D. K. Wilson, V. E. Ostashev, S. L. Collier, N. P. Symons, D. F. Aldridge, and D. H. Marlin. Time-domain calculations of sound interactions with outdoor ground surfaces. *Applied Acoustics*, 68(2):173–200, 2007.